ACS OMEGA

Open Access

http://pubs.acs.org/journal/acsodf

Article

Quantitative Characterization of Inorganic Pores in Sinian Doushantou Dolomitic Shale Based on FIB-SEM in Western Hubei Province, China

Yinan Liu, Peng Zong,* Li Wang, Yanyong Xu, Jingzhen Guo, and Heng Wu

Cite This: *ACS Omega* 2024, 9, 8151−8161

Read Online

ACCESS | Metrics & More | Article Recommendations

ABSTRACT: Unlike traditional shale gas reservoirs, where organic matter pores dominate, inorganic pores are the primary reservoir space in the Sinian (Ediacaran) high-maturity Doushantou dolomitic shale in western Hubei Province, China. The inorganic pore characteristics of Doushantuo shale and its influence on shale gas aggregation were investigated by examining the TOC content, thermal maturity, mineralogical composition, and field-emission scanning electron microscopy (SEM) and focused ion beam scanning electron microscopy (FIB-SEM) of drill cores. The results show that the shale mineral composition in the study area is primarily dolomite and plate-shaped interparticle−intercrystalline pores associated with dolomite are widespread inorganic pores in dolomitic shale. Interparticle−intercrystalline pores account for 75% of the total pores, with a pore size distribution mainly between 50 and 300 nm, as extracted from the 3D pore network model (PNM). Compared with organic pores, interparticle−intercrystalline pores provide greater space for gas storage and have a strong coupling relationship with the hydrocarbon generation and evolution of organic matter. Therefore, the inorganic pores in the Doushantuo Formation play a vital role in the enrichment and accumulation of shale gas. This study aims to establish a scientific basis for understanding the enrichment mechanism of shale gas in Doushantuo dolomitic shale and other inorganic pore-dominated shales in southern China.

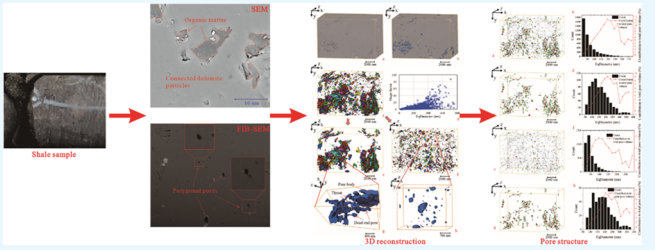

1. INTRODUCTION

Shale gas has gradually become an increasingly significant component of the global energy structure. Pores play a crucial role in storing and transporting shale gas from its storage location to fractures, serving as the primary channel for hydrocarbon migration and accumulation throughout geological history.[1,2] Shale pore types are commonly classified as interparticle pores, intraparticle pores, and organic matter pores.[3]

Numerous studies have demonstrated that organic matter pores are the primary pore type in shale gas reservoirs, including the Barnett shale,[4] Marcellus shale,[5] Woodford shale,[6] Eagle ford shale,[7] and Longmaxi shale.[8] Organic matter pores possess a large surface area and excellent connectivity, facilitating the storage and transport of shale gas.[5,9] In recent years, significant advancements have been made in shale gas exploration, particularly in the Sinian Doushantuo formation in western Hubei, which has become a hotspot for shale gas exploration.[10,11] Previous studies have shown that the Doushantuo shale differs from other shale gas formations, in that it contains over 50% inorganic pores, compared to only 10% in the Longmaxi shale.[12] Due to the high content and wide distribution of inorganic pores in Doushantuo Formation shale, the main types and characteristics of inorganic pores and their significance in shale gas accumulation need more investigation. Currently, the tectonic and sedimentary characteristics of the study area have been determined, along with the distribution and geochemical properties of the Doushantuo shale.[13,14] However, there is limited research on shale pore characteristics.

Pore research methods include fluid invasion and radiation methods. Fluid intrusion methods, such as mercury intrusion, low-temperature nitrogen adsorption, CO_2 adsorption, and nuclear magnetic resonance, rely on molecular probes that enter the pores.[15−18] Therefore, they can measure only connected pores. Radiation methods, such as scanning electron microscopy, transmission electron microscopy, and small-angle scattering, can characterize the connected and nonconnected pores in the shale. The combination of μm-CT and nm-CT or FIB-SEM technology can not only realize three-dimensional imaging of pores but also quantitatively simulate fluid flow

Received: November 1, 2023
Revised: January 17, 2024
Accepted: January 31, 2024
Published: February 8, 2024

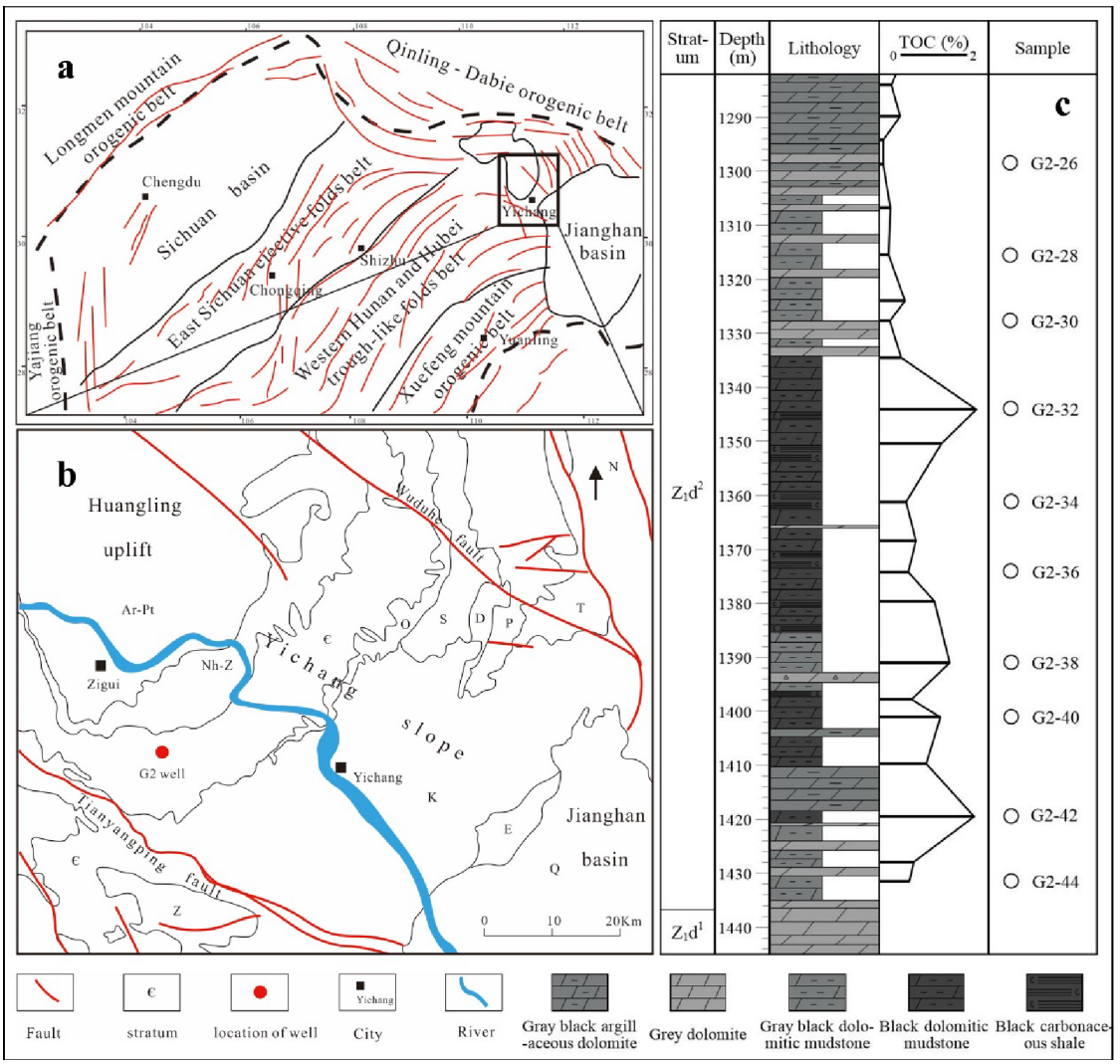

Figure 1. Geological setting of study area. (a) Structural units of the middle Yangtze in southwestern China; (b) a regional diagram of the Yichang slope;[11] (c) stratigraphic column of the Doushantuo Formation in G2 well showing sampled horizons. (Adapted with permission from [reference 11]. Copyright [2019] [Elsevier].).

characteristics in nanopores. This technique has been widely used in tight reservoirs such as coal and shale.[19−21] FIB-SEM has advantages over other experiments in studying pore structures at the three-dimensional nanometer scale due to its high resolution.

This study examines the inorganic pores of Doushantuo shale by using FIB-SEM and other methods. A pore network model was reconstructed using Avizo software to analyze the shape, connectivity, and pore size distribution characteristics of inorganic pores in three dimensions. The significance of inorganic pores in shale gas accumulation was also discussed. This study has significance for other scholars seeking to understand the characteristics and importance of inorganic pores in the Doushantuo shale.

2. GEOLOGICAL SETTING AND SAMPLE

The Yichang slope study area is situated on the southeast side of Huangling uplift, the upper Yangtze plate. During the Indo-Chinese Movement, which took place in the late Jurassic to the early Cretaceous period, complicated fold and fault systems were formed due to the influence of the Qinling-Dabie orogenesis in the northeast and Jiangnan-Xuefeng in the southeast (Figure 1a).[22] Because of the protection provided by the Huangling basement paleo-uplift and the stress relief of boundary faults, the stratum in Yichang slope was not broken.[23] The Sinian and Cambrian strata are visible at the edge of the Huangling uplift (Figure 1b). Shale of the Doushantuo Formation in Sinian was deposited in carbonate plate-basin environment.[13] The lithology consists of dolomitic mudstone and dolomite. Ten core samples were selected from well G2 (Figure 1c). The lithology of samples contains gray-black dolomitic mudstone with lower total organic carbon (TOC) and black dolomitic mudstone and shale with a higher TOC content (Figure 2).

3. METHODS

3.1. TOC Content, Thermal Maturity, and Mineral Components. To investigate the petrological characteristics of the samples, ten sets of total organic content (TOC, wt %), four sets of equivalent vitrinite reflectance, and ten sets of XRD mineralogy analysis were carried out on the crushed samples following the National standards of the people's Republic of China (GB/T) 19145-2003, the Chinese Oil and Gas Industry Standard (SY/T) 5124-2012, and the Chinese Oil and Gas

https://doi.org/10.1021/acsomega.3c08640
ACS Omega 2024, 9, 8151−8161

Figure 2. Sampling points of G2-2 and G2-4 and the lithologic features.

Industry Standard (SY/T) 5163-2010. The equivalent vitrinite reflectance (EqR_o) was converted from the bitumen reflectance (BR_o) according to the equation:[24]

$$\mathrm{Eq}R_o = (\mathrm{B}R_o + 0.2443)/1.0495 \quad (1)$$

3.2. Scanning Electron Microscope Experiment. Samples G2-2 to G2-7 were selected for the SEM experiment. Small pieces, approximately 1 cm^3 in size, were cut from the cores by mechanical cutting machines and then dried at 105 °C for 24 h. The section was observed using the Nova Nano SEM 450 instrument perpendicular to the bedding after carbon plating.

3.3. FIB-SEM Experiment. The SEM observations of ten cores show that all samples contain inorganic pores more or less (details in section 3.2). Therefore, sample G2-5, which has a moderate proportion of these pores, was selected for FIB-SEM experimentation. To make the FIB-SEM imaging field of view more representative, an area that includes the inorganic pores with common characteristics compared with other regions in the wide-scale SEM imaging field of view was selected.

3.3.1. 3D Image Stake Acquisition. A core plug measuring 2.5 cm in diameter and 1 cm in length was extracted from the G2-5 sample. The plug was mechanically polished using dry emery paper to form a flat surface and then milled by argon ion. The sample was then dried for 24 h at a temperature of 105 °C and cooled to room temperature in a sealed container. Carbon was coated on the sample surface to prevent the electrostatic charging effect. The Helios NanoLab 650 FIB-SEM dual-beam system was used for sample cutting and imaging with an ion beam voltage of 30 kV, a current of 0.79 nA, an electron beam voltage of 2 kV, and a current of 0.4 NA. The slice thickness was 20 nm, and the working distance was 4 mm. Holzer[25] et al. provided a detailed description of the instrument composition, cutting and imaging process in detail. During the experiment, the ion beam was perpendicular to the sample surface (that is, parallel to the imaging surface) and the electron beam and ion beam presented a 52° angle, intersecting at the imaging surface of the sample. A group of 600 images with a pixel size of 8.16 × 8 16 nm and a resolution of 2048× 1768 pixels were obtained.

3.3.2. Image Processing. To achieve more accurate image segmentation results, it is necessary to preprocess the raw image data obtained. This includes alining, cropping, compensating for nonuniform illumination, and processing the image (removing noise, enhancing contrast, and sharpening pore edges). The obtained continuous image slice photos were imported into the Avizo software for image processing. The electron beam was at a 52° angle to the imaging surface during the image acquisition process, resulting in foreshortening of the voxel size in the *y*-axis direction of the image and an upward shift in the *y*−*z* plane (Figure 3a). Electron beam

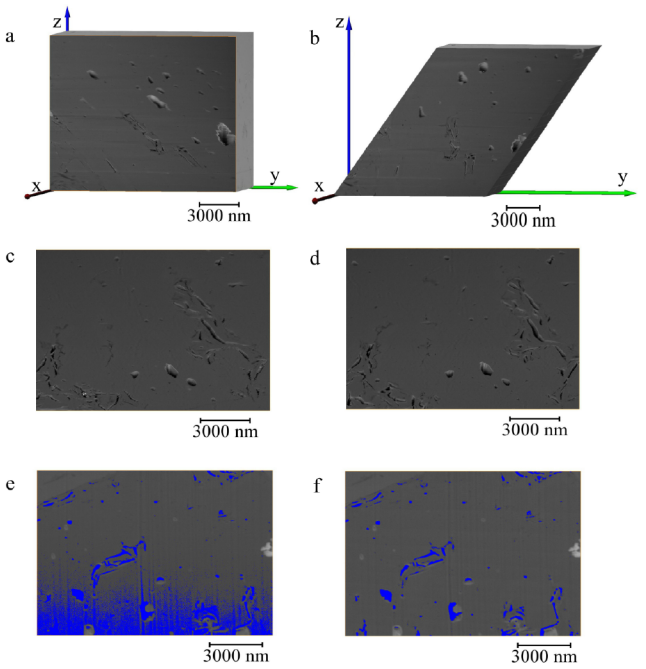

Figure 3. Image processing using FIB Stack Wizard. (a) Raw image stack (parallel *y*−*z*, upward shift in the *y*-direction, pore is elongated); (b) image after alinement (parallel *y*−*z* plane); (c) raw gray level image (parallel *x*−*z* plane, lateral drift led to not smooth pore edges); (d) image after alinement (parallel *y*−*z* plane, pores have smooth edges); (e, f) before and after nonuniform illumination correction (parallel *x*−*y* plane, blue represents a pixel value below 71).

voltage instability and other environmental factors can cause lateral drift of the 3D image-stack, which is most obvious in the *x*−*z* section (Figure 3c). Therefore, the actual size of the voxel in the *y* direction should be $y = y'/\sin(52°) \approx 1.269 \times y'$. Upward shift and drift were corrected by Alinement (Figure 3b,d).[25] In addition, nonuniform illumination phenomena are often present in images (Figure 3e), and a specified value is necessary to normalize the pixel of the 3D image stack to eliminate this phenomenon (Figure 1f). The above steps were completed using the FIB Stack Wizard script module in the Avizo software.

The FIB-SEM image contains numerous physical and nonphysical artifacts. FFT and Fourier-wavelet filtering are effective in removing stripe artifacts,[26,27] while anisotropic diffusion filtering is better for removing salt-and-pepper noise.[28] Other filters that are commonly used in shale FIB-SEM images include median filter, nonlinear means filter[26] and non-local-mean filter.[29] In this paper, the FFT filter was used to remove stripe artifacts and the non-local-mean filter was used to smooth images. The results of the filtering process are shown in Figure 4a,b.

3.3.3. Segmentation. Traditional segmentation methods include multithreshold segmentation based on the Otsu algorithm[30] and watershed segmentation based on the seeded watershed region growing algorithm.[31,32] The segmentation method based on the machine learning algorithm has better application potential.[32−34] Further information on image segmentation can be found in the results published by Schlüter[35] et al. The multithreshold segmentation method

https://doi.org/10.1021/acsomega.3c08640
ACS Omega 2024, 9, 8151−8161

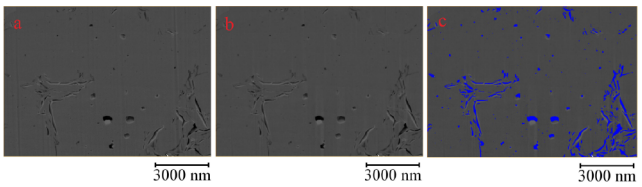

Figure 4. Image processing procedure: (a) image from FIB Stack Wizard (black is void; gray is mineral); (b) filtered image with FFT filter and non-local-mean filter; (c) segmented image (blue is void).

based on the Otsu algorithm was used to segment particles and pores.[30] This method is effective in segmenting pores with lower gray values and solid parts with higher gray values (Figure 4c).

3.3.4. Pore Space Analysis. To analyze the shale pore morphology and distribution, two steps are necessary: volume rendering of pore space and extraction of a pore network model. The binarized image, where the pixel value of the pore space is 1 and the solid voxel is 0, was rendered in Avizo to obtain a three-dimensional geometric model of the pore space. The region of interest (ROI) was extracted by using the Extract Subvolume module for further analysis of the pore structure. Connectivity analysis was conducted on the 3D pore dataset that was separated. Pores that share at least one common vertex were defined as connected pores. The connected pore spaces from the first slice to the last slice in the specified direction (x, y, or z) were extracted. To distinguish between plate-like pores and polyhedral pores, the shape factor ($G = S^3/(36 \times \pi \times V^2)$) was defined. A typical sphere has a shape factor of 1, while a cube has a shape factor of 1.91.

Pore network modeling methods include the erosion-dilation method,[36,37] the maximum ball approach[38,39] and the genetic algorithm.[40] The maximum ball method is considered more accurate than the erosion-dilation method,[38] and easier to operate than the genetic algorithm. Therefore, the Generate Pore Network Module, which is based on the maximum ball method in Avizo software, was used to extract the PNM. Finally, the distribution analysis module was used to perform pore statistical analysis of the pore characteristics, including pore volume, pore surface area, and pore size distribution, as well as throat size and distribution.[9,41]

Note that the ROI and its PNM cannot represent the pore structure of the entire rock sample. They are selected and imaged to characterize interesting nanosized inorganic pores on a three-dimensional scale.

4. RESULTS

4.1. Petrological Characteristics of Shale. The TOC content of well G2 included two higher and two lower layers. The higher values ranged from 1% to 2%, while the lower values were less than 0.5% (Figure 1c). The maturity of the four samples ranged between 2.30%R_o and 2.33%R_o. The shale had generated gas in geological history but currently has little hydrocarbon potential. Table 1 shows the basic characteristics of the shale samples in the study area. The mineral composition of the study area was dominated by dolomite, which had an average content of 69.3%. Siliceous minerals had an average content of 15.9%, while clay minerals accounted for about 11%. Pyrite content was small, with an average of 2.2%, and calcite was almost absent. Unlike other regions, the shale in the study area contained a significant amount of dolomite (Figure 5).

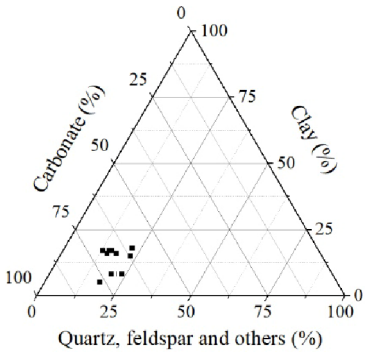

Figure 5. Mineral components of the Doushantuo shales.

4.2. Two-Dimensional Characteristics of Inorganic Pores. The SEM image revealed numerous inorganic pores, including those found between dolomite particles, within dolomite particles, and between dolomite or clay crystals. In shale with lower TOC content, most of the dolomite particles were nonautomorphic and had a large grain size. The particle contact mode was either line contact or suture contact (Figure 6a). Smaller euhedral or semiautomorphic dolomite crystals were present between the larger dolomite particles. Most of the observed pores were located between dolomite crystals and between dolomite crystals and dolomite grains. Those pores were plate-like or wedge-shaped with straight boundaries, intersected at certain angles. The presence of euhedral clay in these pores decreased the pore volume but provided pores

Table 1. Characteristics of Shale Samples

sample	TOC	R_o	dolomite content (%)	siliceous minerals content (%)	clay minerals content (%)	pyrite content (%)	calcite content (%)	feldspar content (%)
G2-1	0.67	–	76	20	4	0	0	0
G2-2	0.17	–	78	11	8	2	0	1
G2-3	0.19	–	67	25	7	1	0	0
G2-4	1.78	2.30	60	22	14	3	0	1
G2-5	0.49	–	70	22	7	1	0	0
G2-6	0.53	–	60	17	17	3	0	3
G2-7	1.29	2.32	66	10	16	4	0	4
G2-8	1.12	2.33	75	7	10	4	0	4
G2-9	1.74	2.33	77	6	12	3	0	2
G2-10	0.55	–	64	19	15	1	1	0
average	0.85	–	69.3	15.9	1.5	2.2	0.1	1.5

https://doi.org/10.1021/acsomega.3c08640
ACS Omega 2024, 9, 8151−8161

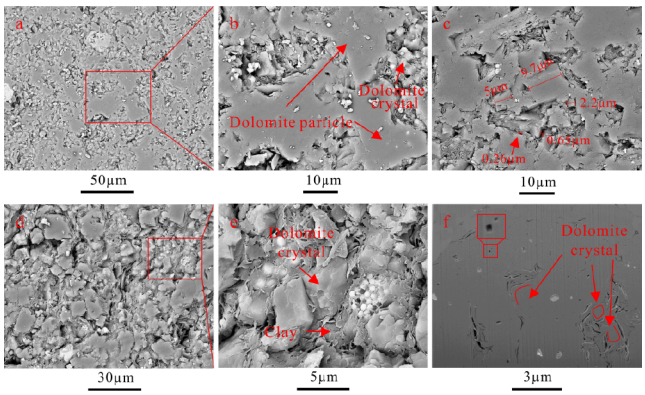

Figure 6. SEM images of samples. a, b, c, and f are from sample G2-3 and G2-5, which have lower TOC than 0.5%, and f is FIB-SEM image slice. d and e are from sample G2-4 which have a higher TOC than 1.5%.

with clay crystals. Additionally, some intraparticle pores were observed in the dolomite particles, which were smaller in size and had a more regular rhombus shape (Figure 6b,c). There was no directionality observed in the distribution of minerals. The shale with a higher TOC content exhibited similar mineral and pore characteristics. In comparison, the particles in the shale with higher TOC were mainly suspended or in point contact, and the shale contained more euhedral or semi-automorphic dolomite and clay crystals (Figure 6d,e).

Loucks[3] et al. defined the pores between particles after crystal cementation as interparticle pores with an intercrystalline appearance. However, the generation relationship between dolomite particles and crystals could not be confirmed, and the size difference between the particles and crystals decreased in the high TOC shale. Therefore, the term interparticle and intercrystalline pore was used directly. The FIB-SEM image showed angular semiautomorphic dolomite crystals. The pores surrounding the dolomite crystals had straight boundaries. The dolomite matrix contained quadrangular or polygonal pores. Affected by the resolution, most of the polygonal pores appeared to be circular (Figure 6f). The gray scale image did not show a significant difference between interparticle pores and intraparticle or intercrystalline pores, so the shape factor was used to distinguish between the two types of pores. It was found that polygonal pores can represent intraparticle pores, while plate-shaped pores can represent both intraparticle and intercrystalline pores. The shape factor of 4 was found to be more effective in distinguishing polyhedral pores from plate-shaped pores, as confirmed by comparing the extracted pores with the original gray scale image.

4.3. Three-Dimensional Characteristics of Inorganic Pores from FIB-SEM. *4.3.1. Pore Geometry.* After preprocessing, the subvolume size was 13.68 μm × 9.08 μm× 9 μm. The volume rendering results are shown in Figure 7a−c. The complexity of the pore structure increased with the pore shape factor, and the pore shape became more similar to a plate shape. In general, the shape factor increased with the increase in pore diameter. The pore shape factors of larger pore sizes had both large and small values (Figure 7d). This suggests that pores with smaller diameters were mainly polyhedral pores, while pores with larger diameters were composed of both polyhedral and plate-shaped pores.

The plate-like pores contributed the majority of the pore volume. Their morphology was complex, and their volume was large (Figure 7e). The pore bodies were connected by narrow throats. Some throats were long and thin tubules or plates, while others were where the pore body narrowed rapidly. Additionally, there were ink-bottle-shaped pores and plate-shaped pores with one end open that were connected to the pore network (Figure 7g). The polyhedral pores were mostly isolated. Due to the influence of image resolution and section thickness, they appeared ellipsoidal and short columnar in three dimensions (Figure 7f,h).

4.3.2. Pore Size Distribution. A total of 4306 pores and 327 throats were extracted from the pore network model (PNM). The average pore volume was 4.6 × 10^6 nm^3 and the total porosity was 1.94%. Plate-shaped pores and locally connected pores had similar quantity, porosity, and size. Plate-shaped pores contributed more porosity, and had larger pore volume but shared fewer numbers compared to polyhedral pores (Table 2). In all of the identified pores, the number of pores decreased significantly with the increase of pore size. Pores with a diameter less than 100 nm accounted for 81.5% of the total number of pores, while pores with a diameter between 100 and 300 nm were the main contributors to the pore space (Figure 8a,b). Plate-like pores and polyhedral pores had different pore size distribution characteristics. The number of plate-like pores increased initially and then decreased as the pore size increased. The diameter of plate-like pores ranged from 100 to 150 nm (Figure 8c,d). The diameter of most polyhedral pores was less than 100 nm, and pores with diameters between 50 and 150 nm contributed to the main pore space of polyhedral pores (Figure 8e,f). The number of plate-like pores was much smaller than the polyhedral pores, but it contributed to most of the pore volume. The polyhedral pores contained only a few large pores.

4.3.3. Connectivity Analysis. The connectivity analysis indicated that there are no connected pores through the sample. 379 locally connected pores and 327 throats were identified by applying a coordination number greater than or equal to 1 (Table 2, Figure 8g). The number of throats of plate-shaped pores accounted for 73.1% of the total throats, and the pore size distribution characteristics of locally connected pores were similar to those of plate-like pores (Figure 8d,h). This indicated that most of the connected pores in the samples were plate-like pores. The coordination number of locally connected plate-like pores was less than 6. As the coordination number increased, the number of pores and pore volume decreased (Figure 9a). The majority of throat diameters were less than 100 nm, with lengths ranging from 200 to 1200 nm. There was no obvious correlation between throat length and 4 throat diameters (Figure 9b).

5. DISCUSSION

5.1. Influence of Test Methods on Results. Resolution is a crucial factor to consider when the image analysis method is used in pore characteristic studies. Only textures larger than the image resolution can be observed. The FIB-SEM image stack used in this study has a pixel size of 16.31 nm × 16 31 nm × 20 nm, so it is unclear whether pores smaller than 20 nm exist. Furthermore, it is worth noting that several pores are linked to subvolume boundaries. It is possible that these pores are interconnected in other regions. Many organic pores obtained in SEM or FIB-SEM experiments may appear to be disconnected, but they are known to be connected at a much smaller scale (below the image resolution).[42] Interparticle pores are considered as the main channel for hydrocarbon

https://doi.org/10.1021/acsomega.3c08640
ACS Omega 2024, 9, 8151−8161

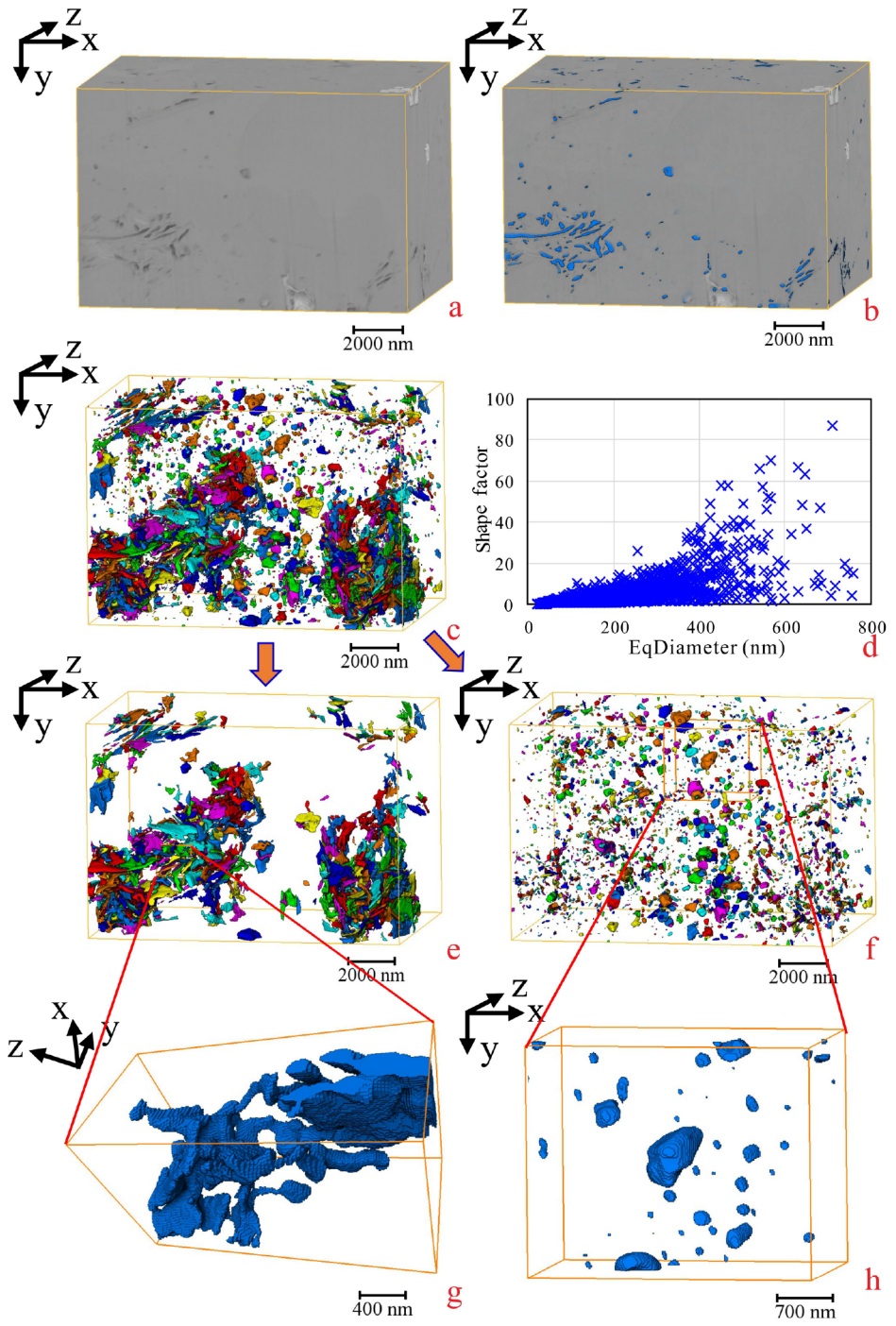

Figure 7. 3D pore network reconstruction and pore shape characteristics. (a, b) Volume rendering of subvolume; (c, d) 3D pore network and its shape factor distribution; (e, g) plate-shaped pores characteristics; (f, h) polyhedral pores characteristics.

Table 2. Pore Characteristics Extracted from PNM

type	porosity (%)	average pore volume (10^7 nm^3)	number of pores	number of throats	judgment
plate-shaped pores	1.46	2.43	677	239	shape factor >4
polyhedral pores	0.48	0.15	3629	24	shape factor <4
locally connected pores	1.13	3.36	379	327	coordination number ≥1
total pores	1.94	0.46	4306	327	–

seepage.[1,2] Therefore, the potential of the plate-like interparticle and intercrystalline pores obtained in this study, which may be connected on a smaller scale, to provide storage and seepage space for natural gas cannot be directly denied. Furthermore, the SEM images of the mechanically polished samples exhibit significantly larger pore contents and sizes compared to the FIB-SEM images. This is attributed to mineral shedding on the sample surface during the sample cutting and

https://doi.org/10.1021/acsomega.3c08640
ACS Omega 2024, 9, 8151−8161

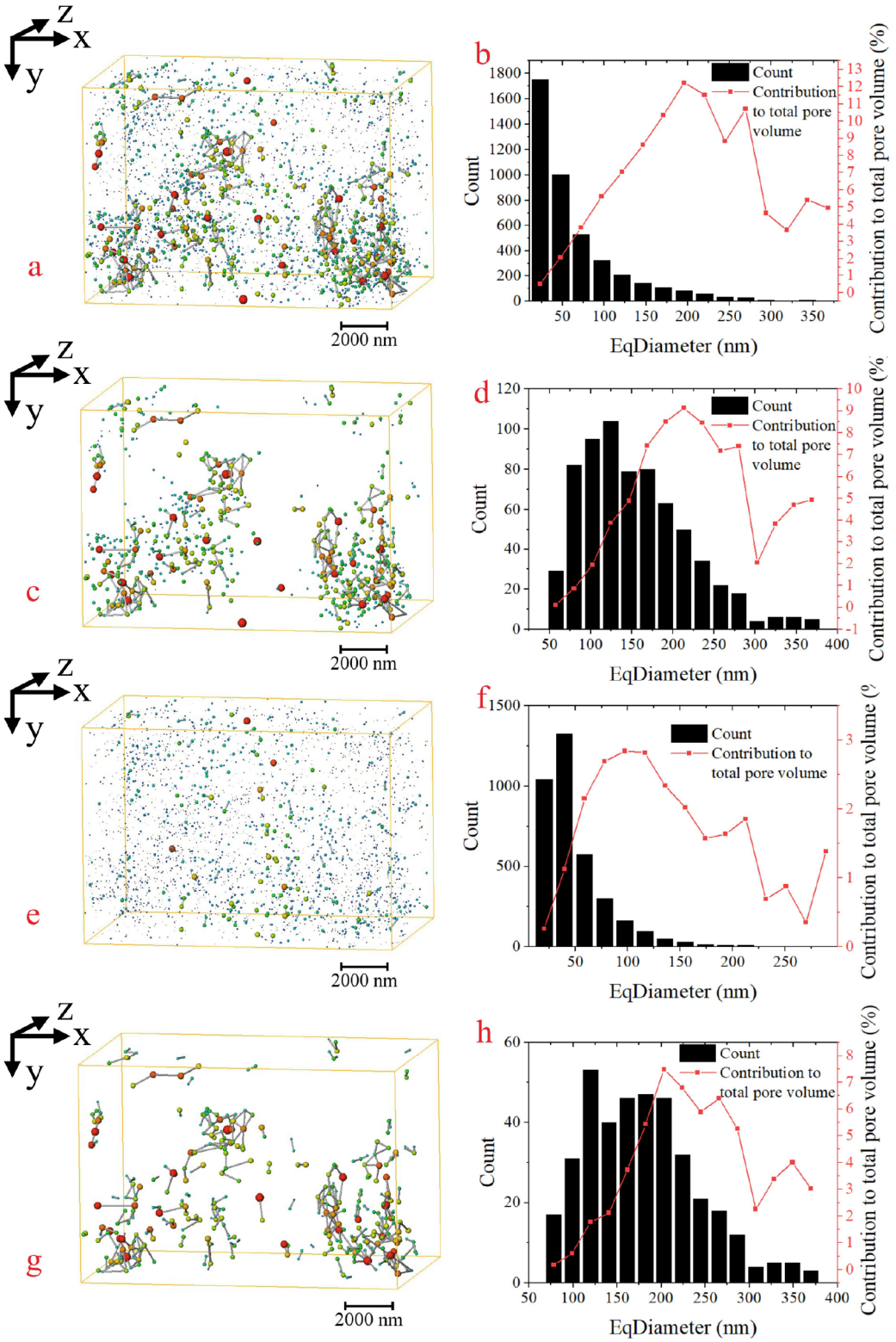

Figure 8. PNM and void distributions. (a, b) Total pores; (c, d) plate-like pores; (e, f) polyhedral pores; (g, h) locally connected pores.

polishing process. However, qualitative information, such as pore type and development location, can still be obtained from cross sections or mechanical polishing surface.

5.2. Comparison between Inorganic Pores and Organic Pores. The sedimentary characteristics of the study area differ from those of other areas, resulting in unique pore types and characteristics of the shale. According to some studies, the pore diameter in clay minerals and organic matters are mainly less than 100 nm, and the number and coordination number of pores is large.[43−46] In this study, the diameter of plate-shaped interparticle and intercrystalline pores is mainly over 100 nm, and the number and coordination number of pores are small (Table 3). Organic pores have a larger specific surface area, providing a greater methane adsorption space. In

https://doi.org/10.1021/acsomega.3c08640
ACS Omega 2024, 9, 8151−8161

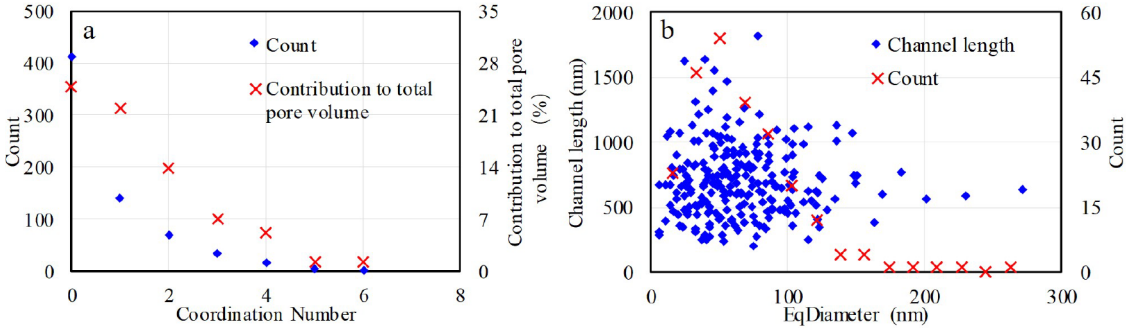

Figure 9. Coordination number distribution (a) and the throat number and length distribution (b) from the PNM of plate-like pores.

Table 3. Main Pore Type and Size of Some Rocks in Previous Studies

author	sample	the main pore types	pore size range
Mengdi Sun[9]	Wufeng shale	organic pore	less than 30 nm
Jan Goral[2]	Vaca Muerta shale	organic pore	less than 75 nm
Shangwen Zhou[43]	Longmaxi shale	organic pore	5−50 nm
C.R. Clarkson[44]	Barnett shale	organic pore	less than 20 nm
Susanne Hemes[41]	boom clay	interparticle and intercrystalline pores	20−100 nm, 3−10 μm
Yang Song[45]	COx claystone	intercrystalline pore	4−6 nm, 50−90 nm
Wenhao Li[46]	Xingouzui argillaceous dolomite	interparticle pore	20−250 nm
this study	Doushantuo shale	interparticle and intercrystalline pores	50−300 nm
this study	Doushantuo shale	intraparticle pore	20−100 nm

contrast, inorganic pores have a larger pore volume and are more likely to serve as a storage space for free gas. Many scholars have defined small pores inside mineral grains as dissolution pores.[42,47] However, in this study, small pores exist in isolated minerals in three dimensions, so the groundwater cannot flow to dissolve minerals. Therefore, they cannot be classified as dissolution pores, and the genesis of the polygonal intraparticle pores remains to be further studied. As these polyhedral pores exist inside the grains and are not connected, they may have no contribution to hydrocarbon storage and migration.

Inorganic pores are formed through deposition and diagenesis, while organic pores are primarily generated through the hydrocarbon production of organic matter. The number and size of organic pores increased gradually because of hydrocarbon generation, and then decreased as a result of compaction during geological history.[48] The evolution of inorganic pores is more complex. No mineral dissolution was observed in the scanning electron microscope images of shale. Without considering the effect of dissolution, the inorganic pores tend to decrease due to compaction and cementation during the evolution process.

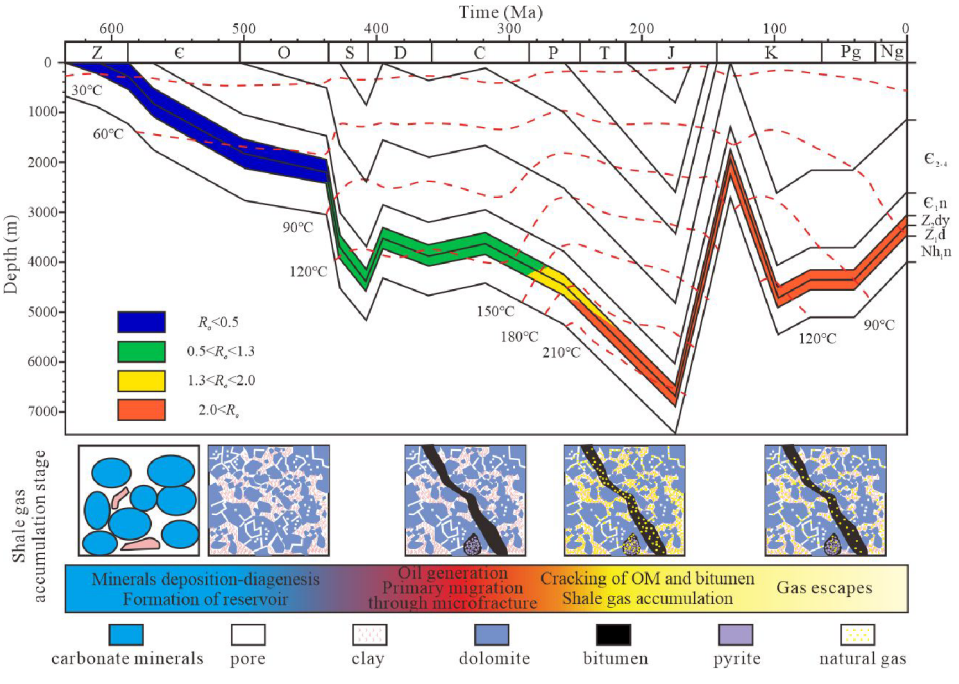

Figure 10. History of maturation thermal evolution and pore characteristics of the Doushantuo Formation shale.

https://doi.org/10.1021/acsomega.3c08640
ACS Omega 2024, 9, 8151−8161

5.3. Relationship between Inorganic Pore Evolution and Gas Accumulation. Recent research indicates that the dolomite formation in the Doushantuo Formation occurred at temperatures below 60 °C,[49] and the Doushantuo Formation dolomite, which is widely found in South China, is syndepositional.[50] Dolomite cements in the Dengying Formation above the Doushantuo Formation were mainly formed during the Paleozoic era.[51] Shale began producing hydrocarbons relatively late, with oil generation beginning around the Silurian period and gas generation beginning around the Permian period (Figure 10). Therefore, the inorganic pores closely related to dolomite in this paper were formed prior to the hydrocarbon generation of organic matter. The shale gas accumulation process in the study area is believed to have occurred in several stages. Prior to the Ordovician period, rocks underwent sedimentary and diagenetic processes, resulting in the formation of a reservoir dominated by inorganic pores formed. From the Silurian to the Carboniferous period, organic matter generated crude oil, some of which remained in shale while some migrated to other strata. The portion retained in the shale may have entered the inorganic pores under pressure. From the Permian period to the Jurassic period, kerogen and crude oil cracked into gas, some of which was trapped in organic matter, while some transported to nearby inorganic pores. Additionally, crude oil that entered inorganic pores during the early stages was also cracked into natural gas. Following the Jurassic period, hydrocarbon generation ceased due to tectonic uplift. However, a significant amount of gas remained in inorganic pores and eventually formed a gas reservoir. Therefore, inorganic pores present in the Doushantuo Formation play a crucial role in the enrichment of shale gas (Figure 10).

Although the inorganic pores of the Doushantuo Formation shale have superior pore content, size, and free gas storage capacity compared to most organic pores, their connectivity is poor. Therefore, reservoir reformation measures, such as fracturing, may still be necessary to increase productivity during the process of exploitation. The inorganic pores observed in this article are mainly between 100 and 300 nm in diameter, which can become effective production channels for shale gas if communicated. Inorganic pores, as a common pore type in shale, must receive the same attention as organic pores.

6. CONCLUSIONS

This paper mainly used SEM and FIB-SEM to investigate the morphology, distribution, and connectivity of inorganic pores developed in the Doushantuo shale in western Hubei. The potential impact of inorganic pores on shale gas was discussed. The following are the main conclusions:

(1) In the study area, dolomite accounts for more than 60% of the Doushantuo shale. Plate-shaped interparticle−intercrystalline pores and polyhedral intraparticle pores associated with dolomite particles and crystals are two kinds of widespread inorganic pore in both high TOC shales and low TOC shales. Interparticle−intercrystalline pores exist between particles or between particles and crystals or between crystals, while intraparticle pores exist in the interior of dolomite.

(2) Interparticle−intercrystalline pores have large plate-shaped pore bodies connected by narrow throats. The pore size distribution of pore bodies mainly ranges from 50 to 300 nm, while the diameter of throats is mainly less than 100 nm. The porosity of interparticle−intercrystalline pores is 1.46%. Intraparticle pores have a porosity of 0.48%, and a pore size distribution mainly ranging from 20 to 100 nm. The number of interparticle−intercrystalline pores is much less than that of intragranular pores, but the pore volume contributed by interparticle−intercrystalline pores is much larger than that of intraparticle pores.

(3) Intraparticle pores are isolated from each other and may have no contribution to gas storage. Interparticle−intercrystalline pores have potential connectivity. Meanwhile, compared to organic pores, interparticle−intercrystalline pores have larger pore size to contribute storage space. These pores have a significant coupling relationship with the gas generation and evolution of organic matter in the geological history, making them an important contributor to the enrichment of shale gas.

AUTHOR INFORMATION

Corresponding Author

Peng Zong − *School of Energy Resources, China University of Geosciences (Beijing), Beijing 100083, China;* orcid.org/0009-0009-5124-4666; Email: zpcugb@163.com

Authors

Yinan Liu − *China United Coalbed Methane Corp., Ltd., Beijing 100011, China*

Li Wang − *China National Offshore Oil Corp., Beijing 100010, China*

Yanyong Xu − *China United Coalbed Methane Corp., Ltd., Beijing 100011, China*

Jingzhen Guo − *CNOOC China Limited, Tianjin 300452, China*

Heng Wu − *School of Energy Resources, China University of Geosciences (Beijing), Beijing 100083, China*

Complete contact information is available at: https://pubs.acs.org/10.1021/acsomega.3c08640

Notes

The authors declare no competing financial interest.

ACKNOWLEDGMENTS

We would like to express our appreciation to the editor and reviewers for their help in revising the article.

REFERENCES

(1) Slatt, R.-M.; O'Brien, N. R. Pore types in the Barnett and Woodford gas shales: Contribution to understanding gas storage and migration pathways in finegrained rocks. *AAPG Bull.* **2011**, *95*, 2017−2030.

(2) Goral, J.; Walton, I.; Andrew, M.; Deo, M. Pore system characterization of organic-rich shales using nanoscale-resolution 3D imaging. *Fuel* **2019**, *258*, 116049.

(3) Loucks, R. G.; Reed, R. M.; Ruppel, S.; Hammes, U. Spectrum of Pore Types and Networks in Mudrocks and a Descriptive Classification for Matrix-Related Mudrock Pores. *AAPG Bull.* **2012**, *96* (6), 1071−1098.

(4) Loucks, R. G.; Reed, R. M.; Ruppel, S.; Jarvie, D. M. Morphology, Genesis, and Distribution of Nanometer-Scale Pores in Siliceous Mudstones of the Mississippian Barnett Shale. *J. Sediment. Res.* **2009**, *79* (12), 848−861.

https://doi.org/10.1021/acsomega.3c08640
ACS Omega 2024, 9, 8151−8161

(5) Milliken, K. L.; Rudnicki, M.; Awwiller, D. N.; Zhang, T. Organic Matter-Hosted Pore System, Marcellus Formation (Devonian), Pennsylvania. *AAPG Bull.* **2013**, *97* (2), 177−200.
(6) Curtis, M. E.; Cardott, B. J.; Sondergeld, C. H.; Rai, C. S. Development of Organic Porosity in the Woodford Shale with Increasing Thermal Maturity. *Int. J. Coal Geol.* **2012**, *103*, 26−31.
(7) Ko, L. T.; Loucks, R. G.; Ruppel, S. C.; Zhang, T.; Peng, S. Origin and Characterization of Eagle Ford Pore Networks in the South Texas Upper Cretaceous Shelf. *AAPG Bull.* **2017**, *101* (03), 387−418.
(8) Hu, G.; Pang, Q.; Jiao, K.; Hu, C.; Liao, Z. Development of Organic Pores in the Longmaxi Formation Overmature Shales: Combined Effects of Thermal Maturity and Organic Matter Composition. *Mar. Pet. Geol.* **2020**, *116*, 104314.
(9) Sun, M.; Zhang, L.; Hu, Q.; Pan, Z.; Yu, B.; Sun, L.; Bai, L.; Fu, H.; Zhang, Y.; Zhang, C.; et al. Multiscale connectivity characterization of marine shales in southern China by fluid intrusion, small-angle neutron scattering (SANS), and FIB-SEM. *Mar. Pet. Geol.* **2020**, *112*, 104101.
(10) Dai, J.; Dong, D.; Ni, Y.; Hong, F.; Zhang, S.; Zhang, Y.; Ding, L. Several essential geological and geochemical issues about shale gas research in China. *J. Nat. Gas Geosci.* **2020**, *5* (4), 169−184.
(11) Zhai, G.; Wang, Y.; Liu, G.; Zhou, Z.; Bao, S.; Chen, K.; Kang, H.; Zhang, J.; Wang, S.; Zhang, Y. The Sinian-Cambrian formation shale gas exploration and practice in southern margin of Huangling paleo-uplift. *Mar. Pet. Geol.* **2019**, *109*, 419−433.
(12) Zhai, G.; Wang, Y.; Zhou, Z.; Liu, G.; Yang, Y.; Li, J. "Source-Diagenesis-Accumulation" enrichment and accumulation regularity of marine shale gas in southern China. *China Geol.* **2018**, *1* (3), 319−330.
(13) Wang, Z.; Liu, J.; Jiang, H.; Huang, S.; Wang, K.; Xu, Z.; Jiang, Q.; Shi, S.; Ren, M.; Wang, T. Lithofacies paleogeography and exploration significance of Sinian Doushantuo depositional stage in the middle-upper Yangtze region, Sichuan Basin, SW China. *Pet. Explor. Dev.* **2019**, *46* (1), 41−53.
(14) Zhu, B.; Jiang, S.; Pi, D.; Ge, L.; Yang, J. Trace Elements Characteristics of Black Shales from the Ediacaran Doushantuo Formation, Hubei Province, South China: Implications for Redox and Open vs. Restricted Basin Conditions. *J. Earth Sci.* **2018**, *29* (2), 342−352.
(15) Clarkson, C.-R.; Jensen, J.-L.; Chipperfield, S. Unconventional gas reservoir evaluation: What do we have to consider? *J. Nat. Gas Sci. Eng.* **2012**, *8*, 9−33.
(16) Xin, F.; Xu, H.; Tang, D.; Cao, L. An improved method to determine accurate porosity of low-rank coals by nuclear magnetic resonance. *Fuel Process. Technol.* **2020**, *205*, 106435.
(17) Xu, H.; Tang, D.; Chen, Y.; Ming, Y.; Chen, X.; Qu, H.; Yuan, Y.; Li, S.; Tao, S. Effective porosity in lignite using kerosene with low-field nuclear magnetic resonance. *Fuel* **2018**, *213*, 158−163.
(18) Xu, H.; Tang, D.; Zhao, J.; Li, S. A precise measurement method for shale porosity with low-field nuclear magnetic resonance: a case study of the Carboniferous-Permian strata in the Linxing area, eastern Ordos Basin, China. *Fuel* **2015**, *143*, 47−54.
(19) Wang, Y.; Yuan, Y.; Rahman, S.-S.; Arns, C. Semi-quantitative multiscale modelling and flow simulation in a nanoscale porous system of shale. *Fuel* **2018**, *234*, 1181−1192.
(20) Wang, M.; Wang, J.; Tao, S.; Tang, D.; Wang, C.; Yi, J. Quantitative characterization of void and demineralization effect in coal based on dual-resolution X-ray computed tomography. *Fuel* **2020**, *267*, 116836.
(21) Goral, J.; Miskovic, I.; Gelb, J.; Andrew, M. Correlative XRM and FIB-SEM for (Non)Organic Pore Network Modeling in Woodford Shale Rock Matrix; International Petroleum Technology Conference: Doha, Qatar, 2015. DOI:
(22) Mei, L. F.; Dai, S. W.; Shen, C. B.; Tang, J. G. Formation and Disintegration of Mesozoic-Cenozoic Intra-Continental Ramp Zone in Middle and Lower Yangtze Region. *Geol. Sci. Technol. Inf.* **2008**, *27* (4), 1−7.
(23) Junfeng, Z.; Hao, X.; Zhi, Z.; Pengfei, R.; Jingzhen, G.; Qiong, W. Geological characteristics of shale gas reservoir in Yichang area,western Hubei. *Acta Petrolei Sinica* **2019**, *40* (8), 887.
(24) Schoenherr, J.; Littke, R.; Urai, J.-L.; Kukla, P.-A.; Rawahi, Z. Polyphase thermal evolution in the Infra-Cambrian Ara Group (South Oman Salt Basin) as deduced by maturity of solid reservoir bitumen. *Org. Geochem.* **2007**, *38* (8), 1293−1318.
(25) Holzer, L.; Indutnyi, F.; Gasser, P.-H.; Münch, B.; Wegmann, M. Three-dimensional analysis of porous $BaTiO_3$ ceramics using FIB nanotomography. *J. Microsc.* **2004**, *216* (Pt 1), 84−95.
(26) Kelly, S.; El-Sobky, H.; Torres-Verdín, C.; Balhoff, M.-T. Assessing the utility of FIB-SEM images for shale digital rock physics. *Adv. Water Resour.* **2016**, *95*, 302−316.
(27) Münch, B.; Trtik, P.; Marone, F.; Stampanoni, M. Stripe and ring artifact removal with combined wavelet:Fourier filtering. *Opt. Express* **2009**, *17*, 8567−8591.
(28) Hosssain, Z.; Ouml, T.-M. Edge Aware Anisotropic Diffusion for 3D Scalar Data. *IEEE Trans. Vis. Comput. Graph* **2010**, *16* (6), 1376−1385.
(29) Buades, A.; Coll, B.; Morel, J.-M. A Non-Local Algorithm for Image Denoising. In *IEEE Computer Society Conference on Computer Vision and Pattern Recognition*; IEEE, 2005; pp 60−65.DOI:
(30) Otsu, N. A Threshold Selection Method from Gray-Level Histograms. *IEEE Trans. Syst. Man Cybern.* **1979**, *9* (1), 62−66.
(31) Münch, B.; Gasser, P.; Holzer, L.; Flatt, R. FIB-Nanotomography of Particulate Systems—Part II: Particle Recognition and Effect of Boundary Truncation. *J. Am. Ceram. Soc.* **2006**, *89* (8), 2586−2595.
(32) Jones, A.-C.; Arns, C.-H.; Sheppard, A.-P.; Hutmacher, D.-W.; Milthorpe, B.-K.; Knackstedt, M.-A. Assessment of bone ingrowth into porous biomaterials using MICRO-CT. *Biomaterials* **2007**, *28* (15), 2491−2504.
(33) Berg, S.; Saxena, N.; Shaik, M.; Pradhan, C. Generation of ground truth images to validate micro-CT image-processing pipelines. *Leading Edge* **2018**, *37* (6), 412−420.
(34) Andrew, M. A quantified study of segmentation techniques on synthetic geological XRM and FIB-SEM images. *Comput. Geosci.* **2018**, *22* (6), 1503−1512.
(35) Schlüter, S.; Sheppard, A.; Brown, K.; Wildenschild, D. Image processing of multiphase images obtained via X-ray microtomography: A review. *Water Resour. Res.* **2014**, *50* (4), 3615−3639.
(36) Lindquist, W.-B.; Venkatarangan, A. Investigating 3D Geometry of Porous Media from High Resolution Images. *Phys. Chem. Earth, Part A: Solid Earth and Geodesy* **1999**, *24* (7), 593−599.
(37) Lindquist, W.-B.; Venkatarangan, A.; Dunsmuir, J.; Wong, T.-F. Pore and throat size distributions measured from synchrotron X-ray tomographic images of Fontainebleau sandstones. *J. Geophys. Res.: Solid Earth* **2000**, *105* (B9), 21509−21527.
(38) Blunt, M.-J.; Dong, H. Pore-network extraction from micro-computerized-tomography images. *Phys. Rev. E: Stat., Nonlinear, Soft Matter Phys.* **2009**, *80*, 036307.
(39) Silin, D.; Patzek, T. Pore space morphology analysis using maximal inscribed spheres. *Phys. A* **2006**, *371* (2), 336−360.
(40) Nejad Ebrahimi, A.; Jamshidi, S.; Iglauer, S.; Boozarjomehry, R.-B. Genetic algorithm-based pore network extraction from micro-computed tomography images. *Chem. Eng. Sci.* **2013**, *92*, 157−166.
(41) Hemes, S.; Desbois, G.; Urai, J.-L.; Schröppel, B.; Schwarz, J.-O. Multi-scale characterization of porosity in Boom Clay (HADES-level, Mol, Belgium) using a combination of X-ray μ-CT, 2D BIB-SEM and FIB-SEM tomography(Article). *Microporous Mesoporous Mater.* **2015**, *208*, 1−20.
(42) Wu, J.; Yuan, Y.; Niu, S.; Wei, X.; Yang, J. Multiscale characterization of pore structure and connectivity of Wufeng-Longmaxi shale in Sichuan Basin, China. *Mar. Pet. Geol.* **2020**, *120*, 104514.
(43) Zhou, S.; Yan, G.; Xue, H.; Guo, W.; Li, X. 2D and 3D nanopore characterization of gas shale in Longmaxi formation based on FIB-SEM. *Mar. Pet. Geol.* **2016**, *73*, 174−180.

https://doi.org/10.1021/acsomega.3c08640
ACS Omega 2024, 9, 8151−8161

(44) Clarkson, C.-R.; Solano, N.; Bustin, R.-M.; Bustin, A.-M.-M.; Chalmers, G.-R.-L.; He, L.; Melnichenko, Y.-B.; Radlinski, A.-R.; Blach, T.-B. Pore structure characterization of North American shale gas reservoirs using USANS/SANS, gas adsorption, and mercury intrusion. *Fuel* **2013**, *103*, 606−616.
(45) Song, Y.; Davy, C.-A.; Troadec, D.; Blanchenet, A.-M.; Skoczylas, F.; Talandier, J.; Robinet, J.-C. Multi-scale pore structure of COx claystone: Towards the prediction of fluid transport. *Mar. Pet. Geol.* **2015**, *65*, 63−82.
(46) Li, W.; Wang, W.; Lu, S.; Xue, H. Quantitative characterization on shale-hosted oil reservoir: A case study of argillaceous dolomite reservoir in the Jianghan Basin. *Fuel* **2017**, *206*, 690−700.
(47) Yang, W.; He, S.; Zhai, G.; Tao, Z.; Dong, T.; Han, Y.; Chen, K.; Wei, S. Pore characteristics of the lower Sinian Doushantuo Shale in the Mid-Yangtze Yichang area of China: Insights into a distinct shale gas reservoir in the Neoproterozoic formation. *J. Nat. Gas Sci. Eng.* **2020**, *73*, 103085.
(48) Zou, C.; Dong, D.; Wang, Y.; Li, X.; Huang, J.; Wang, S.; Guan, Q.; Zhang, C.; Wang, H.; Liu, J.; et al. Shale gas in China: Characteristics, challenges and prospects (I). *Pet. Explor. Dev.* **2015**, *42* (6), 753−767.
(49) Chang, B.; Li, C.; Liu, D.; Foster, I.; Tripati, A.; Lloyd, M.-K.; Maradiaga, I.; Luo, G.; An, Z.; She, Z.; et al. Massive formation of early diagenetic dolomite in the Ediacaran ocean: Constraints on the "dolomite problem. *Proc. Natl. Acad. Sci. U. S. A.* **2020**, *117* (25), 14005.
(50) Cui, H.; Kaufman, A.-J.; Xiao, S.; Zhou, C.; Liu, X.-M. Was the Ediacaran Shuram Excursion a globally synchronized early diagenetic event? Insights from methane-derived authigenic carbonates in the uppermost Doushantuo Formation, South China. *Chem. Geol.* **2017**, *450*, 59−80.
(51) Shen, A.; Hu, A.; Cheng, T.; Liang, F.; Pan, W.; Feng, Y.; Zhao, J. Laser ablation in situ U-Pb dating and its application to diagenesis-porosity evolution of carbonate reservoirs. *Pet. Explor. Dev.* **2019**, *46* (6), 1127−1140.

https://doi.org/10.1021/acsomega.3c08640
ACS Omega 2024, 9, 8151−8161